

## Chapter 16

# Thin epitaxial oxide films as model systems for electrocatalysts

**M.J. Montenegro<sup>a</sup>, T. Lippert<sup>a,\*\*</sup>, S. Müller<sup>b</sup>, A. Weidenkaff<sup>c</sup>, and A. Wokaun<sup>a</sup>**

<sup>a</sup> Paul Scherrer Institute, CH-5232 Villigen PSI, Switzerland

<sup>b</sup> Euresearch, Effingerstr. 19 CH-3001, Bern, Switzerland

<sup>c</sup> University of Augsburg, Universitätstr. 1 D-86159, Augsburg, Germany

## 1. INTRODUCTION

Metal oxides, with an empirical formula  $ABO_3$ , often adopt the so called perovskite structure. This structure type derive its name from the mineral “perovskite”, with the chemical composition  $CaTiO_3$ . The cubic modification of this material is referred to as ideal perovskite, and has a unit cell edge of approximately  $4\text{\AA}$ . In reality, only a few perovskite-type materials have this ideal cubic structure at room temperature, but many reach it at higher temperatures [1]. Distortions from the cubic symmetry produce tetragonal, orthorhombic, and rhombohedral structures. In the face centered cubic (FCC)

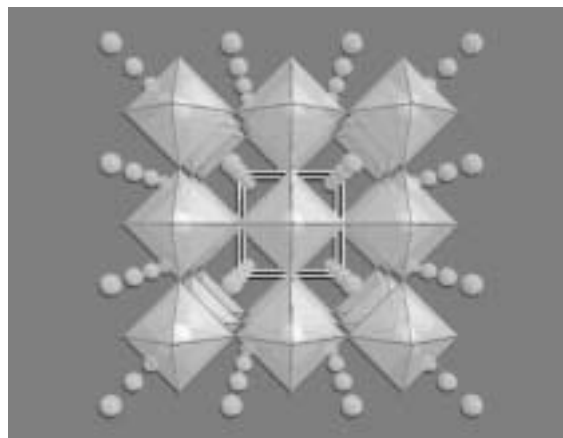


Fig. 1. Perovskite cubic structure.

---

\* Corresponding Author phone ++41-56-3104076, fax ++41-56-3102485, e-mail [thomas.lippert@psi.ch](mailto:thomas.lippert@psi.ch)

structure the *A cations* are located at the corners while the O atoms are on the faces. The *B cation* is in the center of the unit cell (Fig. 1). The corner shared  $\text{BO}_6$  octahedra form a three dimensional network with slightly bigger A-cations in between.

A tolerance factor  $t$  was defined by Goldschmit [2] to describe the stability limits of the perovskite structure (Eq. (1)).

$$t = (R_A + R_O) / 2^{1/2} (R_B + R_O) \quad (1)$$

where  $R_A$ ,  $R_B$  and  $R_O$  are the ionic radii. The perovskite is stable within the range of  $0.75 < t < 1.0$  with  $t$  normally between 0.8 and 0.9. The stable structures below this limit are ilmenite and corundum [3]. The perovskite structure possesses a very high degree of compositional flexibility, which allows to accommodate a wide variety of A and B cations (Fig. 2). In some complex composition the A and B sites can be occupied by more than one cation species ( $\text{A}_{1-x}\text{A}'_x\text{B}_{1-y}\text{B}'_y\text{O}_3$ ). This can involve cations of more than one element, or two oxidation states of the same element.

The physical properties of the perovskite-type materials, such as ferroelectric, dielectric, pyroelectric, and piezoelectric behaviour, will depend on the cation ordering, anion vacancies, and changes in the structural dimensionality. Several examples of perovskite-phases with special properties for various applications are compiled in Table 1. In addition to these interesting physical properties numerous important chemical properties are observed, including catalytic activity and oxygen transport capability. The catalytic activity covers reactions such as CO oxidation, NO reduction, CO and  $\text{CO}_2$  hydrogenation,  $\text{SO}_2$  reduction and various electro-photocatalytic reactions [4]. Some perovskites, i.e.  $\text{La}_{1-x}\text{Sr}_x\text{MnO}_3$ ,  $\text{La}_{1-x}\text{Sr}_x\text{Co}_{1-y}\text{Fe}_y\text{O}_3$ ,  $\text{SrCeO}_3$  and  $\text{SrTiO}_3$  are used for oxygen transport applications (e.g. in gas diffusion electrodes).

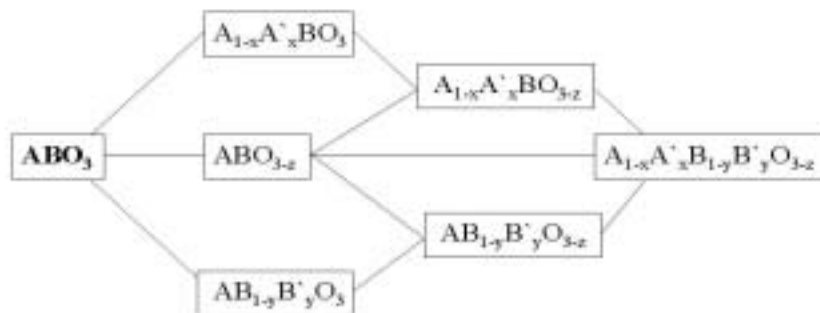


Fig. 2. Various possible compositions of perovskite type-oxides.

Table 1  
Examples for the application of perovskite phases

Multilayer Capacitor	BaTiO <sub>3</sub>
Piezoelectric Transducer	Pb (Zr, Yb) O <sub>3</sub>
P. T. C. Thermistor	BaTiO <sub>3</sub>
Electrooptical Modulator	(Pb, La) (Zr, Ti) O <sub>3</sub>
Switch	LiNbO <sub>3</sub>
Dielectric Resonator	BaZrO <sub>3</sub>
Thick Film Resistor	BaRuO <sub>3</sub>
Ferromagnet	(Ca, La) MnO <sub>3</sub>
Refractory Electrode	LaCoO <sub>3</sub>
Bifunctional Electrode	La <sub>0.6</sub> Ca <sub>0.4</sub> CoO <sub>3</sub>
Solid Oxide Fuel Cells	La <sub>1-x</sub> Sr <sub>x</sub> CoO <sub>3</sub>

The perovskite structure is one of the most important structure classes in material science due to all of these exceptional physical and chemical properties. The ongoing research does not only cover the study of magnetic and electronic properties [5], but also the development of new materials to optimize renewable energy sources, i.e. solid oxide fuel cells [6], direct methanol fuel cells, and metal/air batteries [7]. One of the most important topic for the production of electrochemical batteries is the development of new materials for anodes and cathodes. These materials have to be stable under operation conditions (acidic or alkaline medium with an applied potential), and should be cheaper than the commonly used noble metal materials.

The investigations of rechargeable metal-air batteries started in the early 1970s on power sources for electrical vehicles [8]. However, one major problem associated with the development of these secondary batteries is the limited lifetime of the bifunctional electrode (which catalyzes the reduction and the evolution of oxygen). The lifetime of this electrode is controlled by the dissolution of the catalyst in the electrolyte [9] and the corrosion of the support material (carbon). Progress has been made in the development of corrosion resistant carbon, e.g. carbon nanotubes [10], as support material for the electrodes [11]. Nevertheless, the development of a stable catalyst is still a challenging task. Only few catalysts are intrinsically bifunctional to act as catalysts for both oxygen reactions. Most of the catalysts exhibit either a low catalytic activity or they are unstable under operating conditions [12, 13]. Various catalysts such as noble metals [14], perovskites, spinel, pyrochlore type

oxides [15-17], organometallic compounds [18], and other materials [19] have been evaluated and various methods have been developed to prepare catalytic powders with high surface areas [20]. In particular, the perovskites containing Co, Fe, Mn and Ni are excellent catalysts for the oxygen evolution (OER) and oxygen reduction reaction (ORR) [21, 22].

The origin of the catalytic activity is not yet fully understood, but several hypothesis have been suggested i) a relation between the catalytic activity and the density of states at the Fermi level [23]; ii) the influence of the metal-oxygen binding energy and the  $\pi$  back bonding from the oxygen to the neighboring cations [24]; iii) the presence of oxygen vacancies [25, 26] and iv) that electrical conductivity and magnetic properties are important [23].

Different mechanisms have also been proposed for the oxygen reduction/evolution reactions with perovskite-type oxides as catalysts, but contradictory results have been published [27, 28]. This is most probably due to the different preparation methods for the catalysts powder and the electrodes.

The best method to overcome this influence is the preparation of electrodes on inactive substrates with well defined electrolyte/oxide interfaces, i.e. model system. This will allow to study and compare the mechanism of the oxygen reduction/evolution reaction of different perovskite oxides without any interference from the support material (carbon), (such as electrochemical activity and stability of the carbon, and the uncertainty about the surface area of the electrode being in contact with the electrolyte due to the porous structure). Another advantage of the model system is the possibility to study the influence of the exposed crystallographic surface planes on the catalytic activity. The best model system will therefore be a dense crystalline films deposited on an inactive substrate.

Various techniques such as molecular beam epitaxy (MBE) [29], chemical vapor deposition (CVD) [30], sputtering (RF, Magnetron, and ion beam) [31], and pulsed laser deposition (PLD) [32-34] have been used to deposit thin films.

The advantages of PLD compared with other deposition techniques are well summarized by Chrisey and Hubler [35]. Briefly, the main advantage of PLD is the flexibility to control different parameters which allows an optimization of the deposition conditions. The arrival rates of atoms on the substrate and the possibility to work with higher pressures of background gases are other important factors. PLD has been successfully used for the growth of many types of multicomponent thin films with a very high quality [36, 37]. Nevertheless, some limitations exist, such as particulates, incongruent ablation and oxygen deficiency in oxide materials. To minimize these limitations some modifications to the traditional PLD have been developed. Some examples for these modifications are Aurora-PLD [38], RF plasma assisted pulsed laser deposition [39, 40], PLD with an electric field applied to the substrate [41], UV assisted PLD [42], off-axis PLD [43], magnetic-field PLD [44], and pulsed reactive crossed-beam laser ablation (PRCLA) [45].

The first report on the combination of a pulsed gas supply with PLD was published by Gupta and Hussey in 1991 [46]. This setup allows the application of low background pressures, which enables the implementation of in situ vacuum characterization techniques, e.g. reflection high-energy electron diffraction (RHEED). The main difference between this setup and the PRCLA setup used in our studies is the distance of the gas pulse to the ablation spot on the target (Fig. 3).

For PRCLA the distance is smaller than  $\approx 10$  mm, which allows an increase of the gas phase interaction and the probability of reactive scattering between the gas pulse and plasma, while the resulting species propagate freely away from the localized scattering region [36]. The advantages of PRCLA compared to PLD were demonstrated by Willmott and Antoni [47] for the growth of GaN films. PRCLA has also been applied successfully [48] for the growth of perovskite films. The films present the correct oxygen stoichiometry without any post-annealing procedure.

The influences of the different deposition parameters during the growth of  $\text{La}_{0.6}\text{Ca}_{0.4}\text{CoO}_3$  thin films are presented in this study. This specific material stoichiometry was selected due to its industrial application as bifunctional catalyst in electrically rechargeable Zn/air batteries [49-51] (Fig. 4). The thin film will be used as a model system to test and optimize the catalytic activity of the bifunctional electrode by evaluating various perovskites.

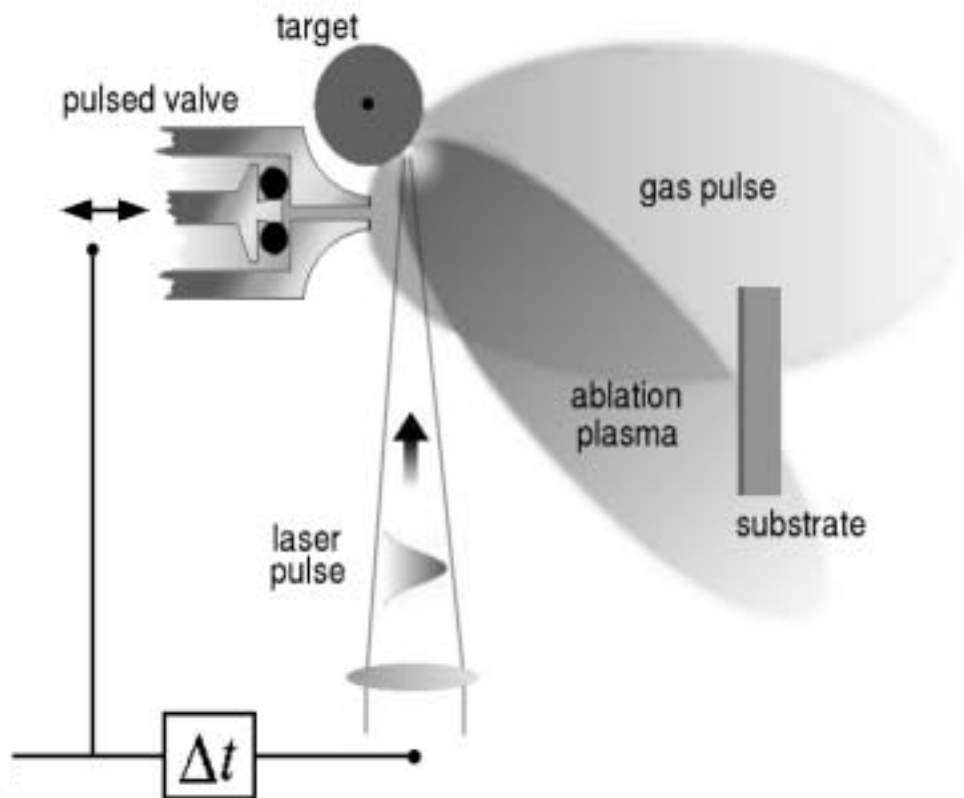


Fig. 3. Pulsed reactive crossed-beam set up.

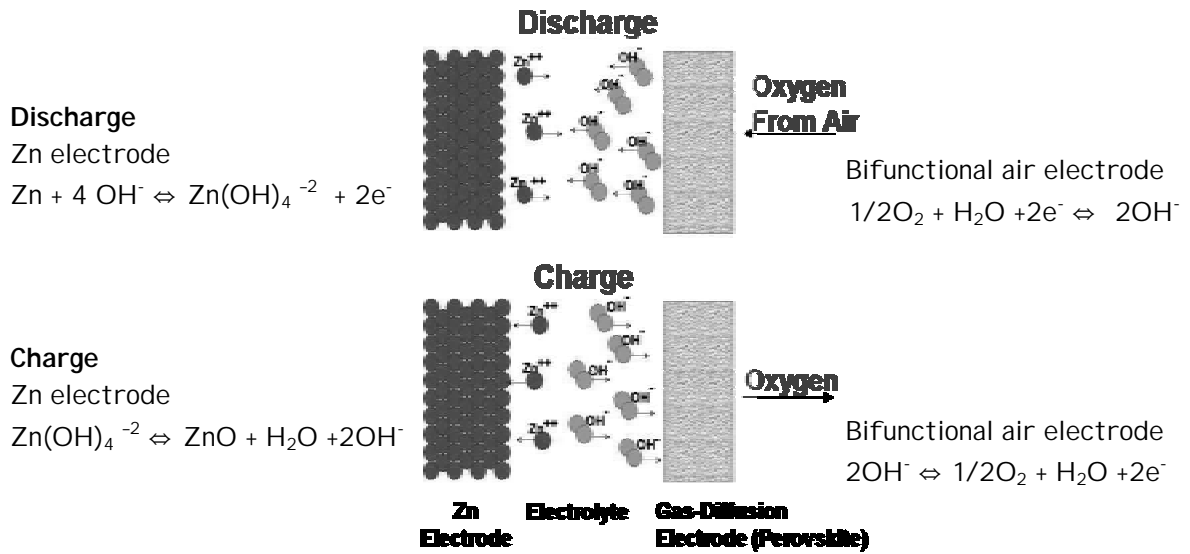


Fig. 4. Scheme of Zn-air battery and reactions involved for each step.

## 2. EXPERIMENTAL

Thin films of  $\text{La}_{0.6}\text{Ca}_{0.4}\text{CoO}_3$  were deposited by ablation of a rotating target, which was sintered from powders prepared by spray pyrolysis. The stoichiometry of the target (i.e.  $\text{La}_{0.6}\text{Ca}_{0.4}\text{CoO}_3$ ) was confirmed by atomic emission spectroscopy. A KrF excimer laser ( $\lambda = 248 \text{ nm}$ ) with a pulse duration of 17 ns was used as irradiation source. The target material in the shape of a rod is located normally at a distance of 4.5 cm from the substrate, but this distance can be varied if necessary. The target was ablated with a laser fluence of  $7.6 \text{ Jcm}^{-2}$  at a repetition rate of 10 Hz with 21,000 pulses for each film. The films were grown on  $\text{MgO}(001)$ ,  $\text{LaAlO}_3(001)$  and stainless steel (Cr-Ni, type SUS 304,  $10 \times 10 \times 0.5 \text{ mm}^3$ ) substrates with one side polished and at a typical temperature of  $650 \text{ }^\circ\text{C}$  (for some experiments this value was changed). The substrates were heated by clamping them to Si substrates, where the rough sides of both were in contact. The Si substrates were ohmically heated by passing a DC current through them. The temperature of the Si substrates was determined by monitoring the resistivity of the Si wafer, which can be compared to reference tables [52]. The substrates were rotating during the deposition to obtain uniform film thickness. Two different oxygen sources were used during

film growth, i.e. from a synchronized pulsed valve operating at a backing pressure of 2 bar N<sub>2</sub>O (99.999 % purity, pulse length of 400 μs) and a leak valve to provide an additional background pressure of O<sub>2</sub> of  $\approx 8 \times 10^{-4}$  mbar during the deposition. The time delay between the gas pulse and the laser pulse was 400 μs, at which the maximum interaction between the ablation plasma and the gas pulse is achieved, as described in detail elsewhere [36]. The films were cooled with a “fast procedure” after the deposition, where the chamber was vented and the films were removed after 15 minutes ( $\approx 40^\circ\text{C}/\text{min}$  cooling rate). The film thickness and surface roughness were determined with a profilometer (Dektak 8000). The morphology of the films was also measured with a Park Scientific Instrument in contact mode. The crystalline structure and texture of the films were determined by a Siemens D5000 X-ray diffractometer with Bragg-Brentano geometry using Cu K $\alpha$  radiation. The apparatus is equipped with an Eulerian cradle for sample orientation. The tubular aperture is limiting the beam divergence of  $0.3^\circ$ . Scans in  $\theta/2\theta$  geometry under different tilt angles were performed using an aperture of 0.2 mm. X-ray pole figures were measured by rotating the sample around the  $\phi$  axis and tilting the sample along the  $\chi$  axis during the measurements with a fixed detector position ( $2\theta$ ). The transmission electron microscopy (TEM) studies were performed on a Phillips CM 30 apparatus equipped with EDX detector. The cross-sectional samples were prepared by cutting two small squares of the sample and gluing those face to face together, after thinning of the samples by mechanical grinding and ion-milling. The film stoichiometry was determined by Rutherford Backscattering Spectroscopy (RBS) measurements using a 2 MeV <sup>4</sup>He beam and a surface barrier silicon detector. The collected data were analyzed using the RUMP program [53].

The plasma formed during the ablation process is analyzed by emission spectroscopy in the range of 300-800 nm. The spectra were collected at different distances from the target, i.e. from 0 to 10 mm and from 40 to 50 mm. The plasma emission is imaged from the plume via a fiber optic to a spectrometer (Acton Research Corporation Spectra Pro-500) with an I-CCD camera (Princeton Instrument, ICCD-1024-MLDG-E/1, EEV 1024 x 256 CCD). Two 1.5 mm wide slits in front of the focusing lens define the region of the observed plasma.

The preparation of the gas diffusion electrodes has been described in detail previously [54]. The electrochemical activity of the LCCO films and gas diffusion electrodes for the oxygen reactions was measured with a three electrodes arrangement with the LCCO as a working electrode, a Pt-wire as counterelectrode, and an Hg/HgO as reference electrode with a potentiostat (Amel instruments, model 2049). The electrodes are submerged in a cell with a 1M solution of KOH. Oxygen is bubbled for saturation through the KOH solution. A potential is applied to the electrode, obtaining the current as an answer, which is normalized for the electrode area (i.e. current density).

### 3. RESULTS AND DISCUSSION

Films produced with fluences under  $12 \text{ Jcm}^{-2}$  present a good quality, where no droplets are observed, independently of the number of applied pulses. The films are dark and shiny if the thickness exceeds 100 nm and they are transparent to visible light if they are thinner. The properties, e.g. conductivity, of the LCCO change as a function of the oxygen content. The most crucial parameter to control during the deposition is therefore the amount of available oxygen to avoid films with oxygen deficiencies. The combination of the oxygen background and the  $\text{N}_2\text{O}$  (strong oxidizing gas) pulse reveals a minimum amount of deficiencies without any enrichment of the other elements. This suggests that in our system congruent ablation occurs contrary to the observations of Boyd et al. [55] for  $\text{La}_{1-x}\text{Ca}_x\text{MnO}_3$  and Craciun et al. [56] for  $\text{La}_{0.5}\text{Sr}_{0.5}\text{CoO}_3$ . The stoichiometry of the films was determined by RBS resulting in a stoichiometry of  $\text{La}_{0.64\pm 0.04}\text{Ca}_{0.35\pm 0.05}\text{Co}_{0.95\pm 0.05}\text{O}_{3\pm 0.21}$  [45].

The influence of the substrate temperature (at a distance of 4.5 cm, Fig. 5A) and the target-substrate distance (at fixed substrate temperature of  $650^\circ\text{C}$ , Fig. 5B) on the stoichiometric indices of LCCO films was studied in detail. These conditions were chosen because films with a defined epitaxial crystallographic orientation were obtained. The measured stoichiometric indices as a function of the process conditions reveal that these changes do not affect the stoichiometry of the films, suggesting that the deposition condition can be varied over a certain range without changing the chemical composition of the films.

The kinetic energy of the particles arriving at the substrate is only slightly decreasing when the temperature is kept constant ( $650^\circ\text{C}$ ) and the distance is in the range of 3.7 to 6.0 cm (from the time- and space-resolved emission spectroscopy data, see below). This is due to the fact that the particles propagate freely in the direction to the substrate without collisions with the oxygen molecules of the background gas ( $8 \times 10^{-4}$  mbar) (mean free path of around 13 cm) after the interaction (collision) zone with the gas pulse molecules.

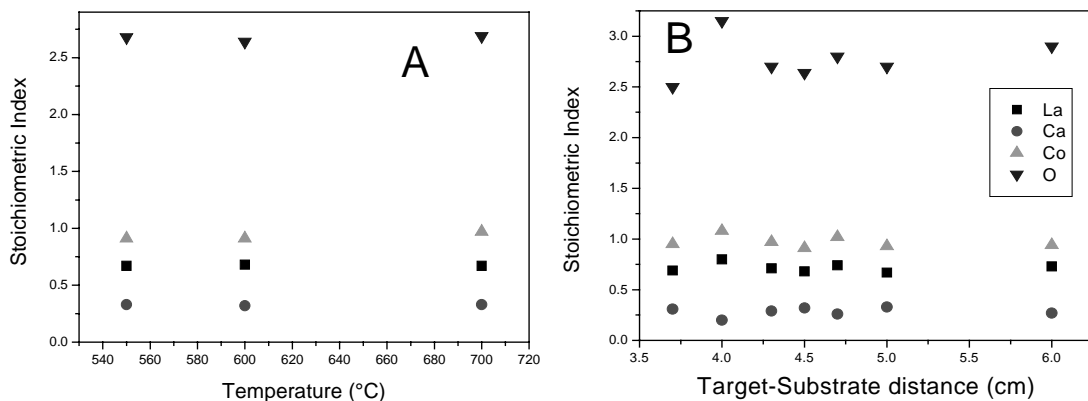


Fig. 5. A: Stoichiometric indices for  $\text{La}_{0.6}\text{Ca}_{0.4}\text{CoO}_3$  films A: at a target-substrate distance of 4.5 cm and B: at  $650^\circ\text{C}$ .

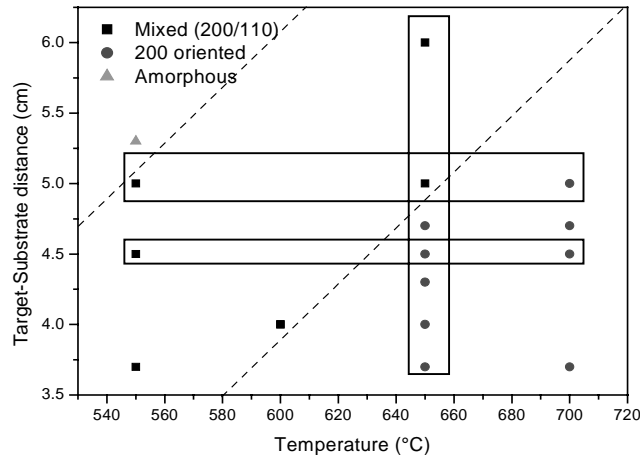


Fig. 6. Influence of the temperature and target-substrate distance on the crystallographic orientation.

The kinetic energy of the atoms arriving at the substrate is between 1.99 to 0.74 eV, which is too small to cause re-sputter of the elements from the growing film [57]. No changes in the stoichiometry are observed when the distance is kept constant (4.5 cm) and the temperature is changed (550°C-700°C). This suggests that there is no pronounced re-evaporation of the elements from the growing film at these temperatures.

As was mentioned above, the crystallinity is a very important parameter, which can influence the catalytic activity. Experiments were therefore performed to determine the influence of the substrate temperature and target-substrate distance on the crystallographic orientation of the film (Fig. 6).

The crystallographic orientation was determined for a given temperature (650°C) and a variable target-substrate distance. A pronounced influence of the distance was observed: the films are only oriented in the (100) direction (same as the substrate) up to a distance of approximately 4.7 cm; further away a mixture of (100/110) orientation is observed. A change in the orientation is also observed when the distance is kept constant at 4.5 cm and the temperature is changed between 550-700°C. At lower temperatures a mixture of the 100/110 orientation is observed, while at higher temperatures the 100 orientation is dominating. At greater distances, e.g. at 5.0 cm a change to single orientations is detected with increasing temperature. This confirms the role of the kinetic energy of the atoms arriving at the substrate. The particle's energy at the substrate which is utilized for film formation (crystallographic structure and morphology) originates mainly from two sources, i.e. the kinetic energy of the arriving particles and from the temperature of the substrate. The substrate temperature is determining the crystallographic orientation when the distance (kinetic energy) is kept constant. An increase of the temperature improves the mobility of the clusters and of arriving atoms. In this case the number of defects is minimized (due to the mobility) and the film growth in the same orientation as

the substrate. The transition temperature from mixed orientation to an unique crystallographic orientation is observed at higher temperatures if the target-substrate distance is increased (to 5 cm), which corresponds to lower kinetic energies.

This behaviour, i.e. the additive effect of the energy from substrate temperature and kinetic energy, is confirmed by the corresponding experiments where the temperature is kept constant while the distance is varied. The transition from a single crystallographic orientation to the films with tilted crystallographic domains is now observed when the distances are increased. A detailed analysis of the influence of distance and temperature reveal, that it is even possible to obtain amorphous films, if low temperatures and large distances are applied. The variation of the two parameter (distance and temperature) gives the unique opportunity to prepare films with crystallographic features that vary between amorphous and single crystalline.

The X-ray diffraction pattern, and the pole figure of a LCCO film deposited on MgO, using the best deposition conditions, (i.e. 650°C at 4.5 cm and using the “fast” cooling procedure), are shown in Figure 7A and 7B. The formation of the crystalline LCCO phase is observed, indicated by an intense Bragg peak at 48.04° which corresponds to the LCCO<200> reflection. Figure 7B shows the (111) pole figure of the LCCO film (at a  $2\theta$  angle of 42.97°). Four maxima at  $\chi=54^\circ$  are observed, indicating the high crystallinity of the deposited film and the cubic structure.

The reproducibility of the crystallinity and the cubic structure was confirmed by varying the substrate, i.e. LaAlO<sub>3</sub>. The X-ray diffraction shows the same single peak corresponding to the LCCO(200) reflection and the pole figure reveals also the four maxima indicative of the cubic structure (not shown).

The growth mechanism of the films and of the LCCO/substrate (MgO and LaAlO<sub>3</sub>) interface was studied by cross sectional TEM (Fig. 8A-B).

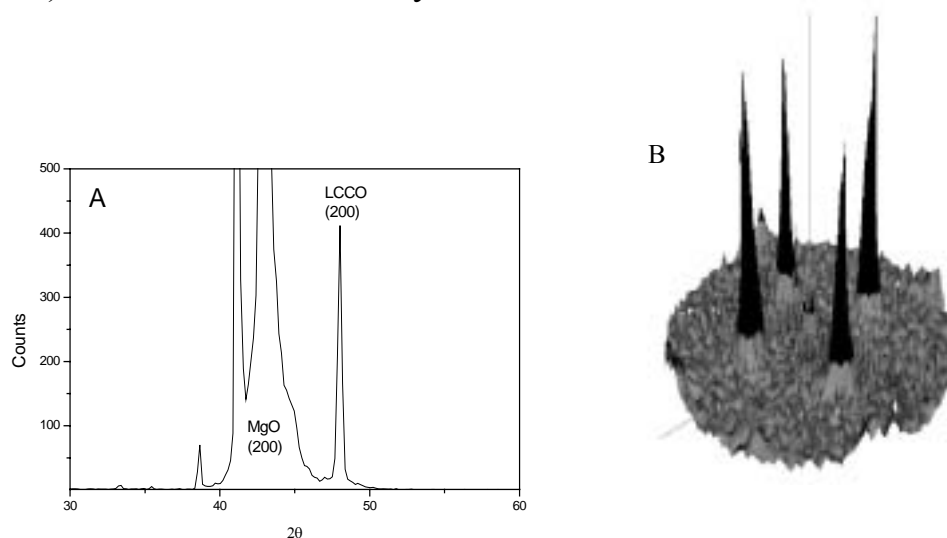


Fig. 7. A: X-ray diffractogram of a LCCO film deposited on MgO(100) and B: pole figure of the same film.

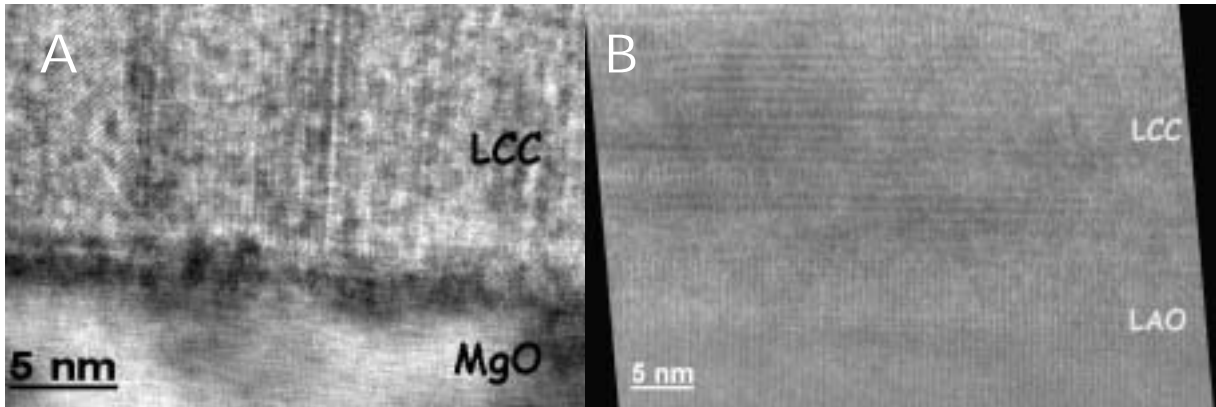


Fig. 8. TEM images of LCCO films A: on MgO(100) and B: on LaAlO<sub>3</sub>(100).

The images reveal that the interface of the films on MgO is much more irregular than in the case of LaAlO<sub>3</sub>. For both substrates the stress during the initial growth is diminishing with increasing film thickness, resulting in both cases in epitaxially grown films. This stress is due to the lattice misfit, i.e. the difference of unit cell size between substrate and film. The example of the LCCO film on LaAlO<sub>3</sub> shows that less stress and defect free interfaces can be obtained when the unit cell size of the film and substrate are matched.

Another important feature for the substrate-film interface, film growth, and quality of the resulting films, is the growth mechanism. The first steps of the growing film were studied for LCCO on MgO substrates. For these experiments the number of pulses was limited to 5-70 which corresponds to a film thickness between 2-10 nm with a lateral size of grain-like features between 2-40 nm diameters. An increase of the pulse number to 500 resulted in an increase of the grain size to  $\approx 100$  nm, which is most probably due to the coalescence of the LCCO islands. A cross-sectional TEM image of a LCCO film grown with 78 pulses is shown in Fig. 9.

A complete coverage of the substrate with a thin film and additional islands of approximately 20-80 nm diameter which are separated by 40-70 nm can be observed. This result indicates that the growth mechanism can either be described by the *Volmer Weber* (growth as islands) or *Stranski-Krastanov* (growth of layer followed by island growth) mechanism.

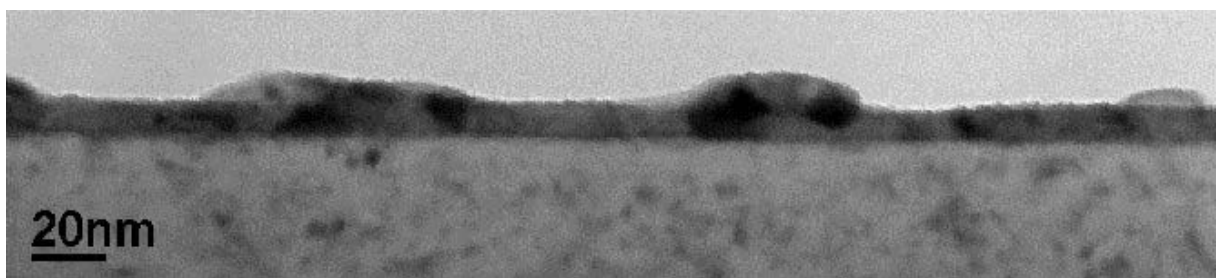


Fig. 9. TEM image of a LCCO film on MgO(100) grown with 78 pulses.

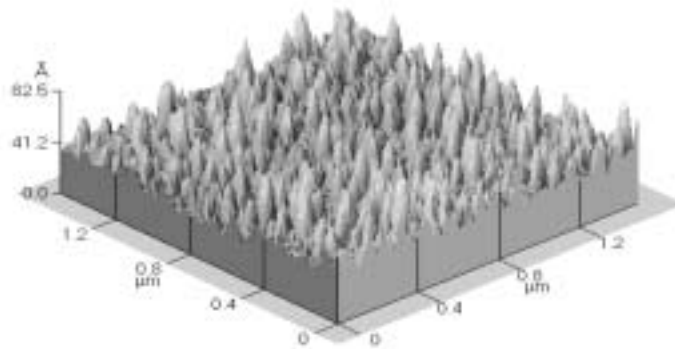


Fig. 10. AFM image of a LCCO film deposited with 5 pulses.

Films prepared with 5, 10, 20, 30 and 50 pulses were measured by AFM to elucidate which of these mechanisms is acting. The image of a film produced with 5 pulses reveals small grain-like structure with a diameter of 2 nm which form a dense layer that may cover the MgO substrate (Fig. 10) completely. With 20 pulses larger grains are observed that form probably already a complete layer. Future TEM measurements will be used to confirm these preliminary data.

The morphology of the films is another parameter that can influence the catalytic activity. Differences in morphologies can result in significant differences in the roughness, which is directly related to the active surface area of the electrode and therefore the catalytic performance. The surface morphology was initially studied as a function of the oxygen source (with the gas pulse alone, only with background gas, and with the combination of both) (Fig. 11), temperature, and target-substrate distance.

When the films are deposited only in the presence of the oxygen background ( $8 \times 10^{-4}$  mbar) a combination between large (25 nm) and small columns (5.7 nm) is observed, where each column may be formed by a single grain. The roughness ( $\approx 7$  nm) of these films obtained from the AFM images is in agreement with the values obtained by the profilometer. For films deposited only with the  $N_2O$  gas pulse (2 bar), smaller grains than in the case of the films obtained by the  $O_2$  background are observed. The average grain size is approximately 17 nm and the roughness of the films is around 6 nm. A lower density of grains with an average size of  $\approx 40$  nm and a roughness of  $\approx 11$  nm is detected when the films are deposited with the combination of both oxygen sources, i.e. PRCLA.

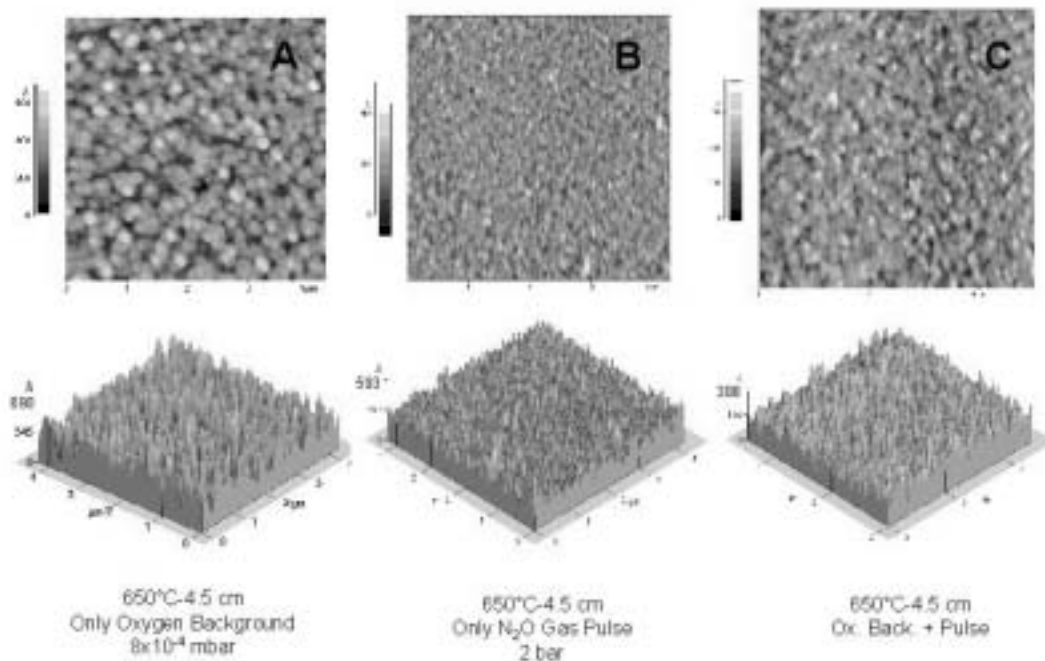


Fig. 11. AFM images of LCCO films deposited A: only with the oxygen background (zone T), B: only with the  $N_2O$  gas pulse (zone I) and C: with oxygen background and gas pulse (PRCLA; zone I with some zone T features,) (note the different height scales).

The variation of morphology for the different conditions can be explained by the “microstructure zones model” of Thornton [58] and its application to PLD [59]. Briefly, the model describes three different types of microstructures and relates the creation mainly to the background pressure, i.e. the kinetic energy and variation of the angle of incidence of the particles on the substrate. The different microstructures are described as:

- 1) Zone II structures, which are very dense structures with a very low roughness. These structures are formed at very low background pressures and with a very small target-substrate distance, i.e. the substrate is placed clearly inside the plume (the importance of the excited state species is not described in detail). These structures are not observed in our conditions.
- 2) Zone T morphology, where large scattered structures are surrounded by smaller structures. These structures are observed for conditions as in 1, but for larger target-substrate distances, or at slightly higher pressures.
- 3) Zone I columnar structures, where a fine fibrous morphology with voids is observed (smaller structures than for zone T). These structures are formed at higher pressures with a large amount of collisions of the particles, which results in a large variation of the incidence angles of the particles arriving on the substrate.

The background pressure of the oxygen (only O<sub>2</sub> background) is so small that almost no collisions occur between the ablated species and the O<sub>2</sub> gas. The ablated particles retain their kinetic energy from the target to the substrate and arrive with a narrow angle of incidence distribution. The resulting films are dense and grow with a bimodal distribution of grain sizes, i.e. large scattered grains surrounded by small grains (*zone T*). Collisions between the ablated material and the gas pulse molecules are important and can be observed by an increase of the plasma emission when the gas pulse is applied with or without the background pressure. The ablated particles arrive at the substrate with a large variety of incidence angles and are partially thermalized before reaching the surface. This induces according to Thornton a “*self shadowing*” effect [60], resulting in the above described *zone I columnar microstructures*. Films grown with the PRCLA method reveal microstructures similar to the *zone I structures*, but with additional *zone T* features. The reason for this intermediate behaviour is not yet clear, but may be a specific feature for the combination of a “high pressure zone” (gas pulse) in a low pressure background.

The previously described models explain the formation of the microstructures mainly for a fixed substrate temperature which is low compared to the melting point of the deposited material. The change from the *zone T* (low pressure) to the *columnar zone I* microstructures is mainly related to the pressure and thus the number of collisions. The larger number of collisions with higher pressures (e.g. the ‘local’ high pressure with the gas pulse) decreases the kinetic energy of the particles and increases the possible angles of incidence of the particles arriving at the surface.

The morphology of films grown with the PRCLA method was also studied as a function of temperature and target-substrate distance under conditions which are typical for the growth of well-defined LCCO films. The results are summarized in Figure 12 and Table 2. The grain dimensions and roughness increase with increasing temperatures for films grown at a fixed target-substrate distance of 4.5 cm. An increase in temperature improves the surface mobility of clusters at the surface, resulting in coalescence of cluster to form larger clusters that are growing even further with the continuing supply of arriving species. For a fixed temperature, i.e. 650°C, and various distances no clear tendency can be observed. An initial increase of the grain size and roughness with increasing distance is observed, which is followed by a decrease of both.

The microstructures for PRCLA (at 650°C and 4.5 cm, shown in Fig. 11c) resemble, as discussed above, a mixture from zone I structure with pronounced zone T features. The structures at other distances (3.7 and 5 cm) and temperatures (550, 650 and 700°C) are shown in Figure 12.

Several general trends can be observed, i.e. with increasing temperatures an increase of the size (height) of the microstructures is observed while for larger distances smaller features are detected, which is most pronounced at the lower temperatures.

Table 2

Influence of temperature and substrate-target distance on the grain size and roughness. R rms corresponds to roughness roots mean square, h corresponds to the height distribution of the particles using the lowest observed point as zero value, and the average grain size corresponds to an average of measurements of height and diameter of single grains (approximately the average of 30 grains for each picture).

Deposition temperature (°C)	Target-substrate distance (cm)	Average grain dimensions (nm)	R rms (Å)	h distribution (Å)
550	4.5	141 x 7	29	95
650	4.5	262 x 12	53	250
700	4.5	237 x 24	99	380
650	3.7	250 x 8	40	150
650	4.5	262 x 12	53	250
650	6.0	165 x 11	43	160

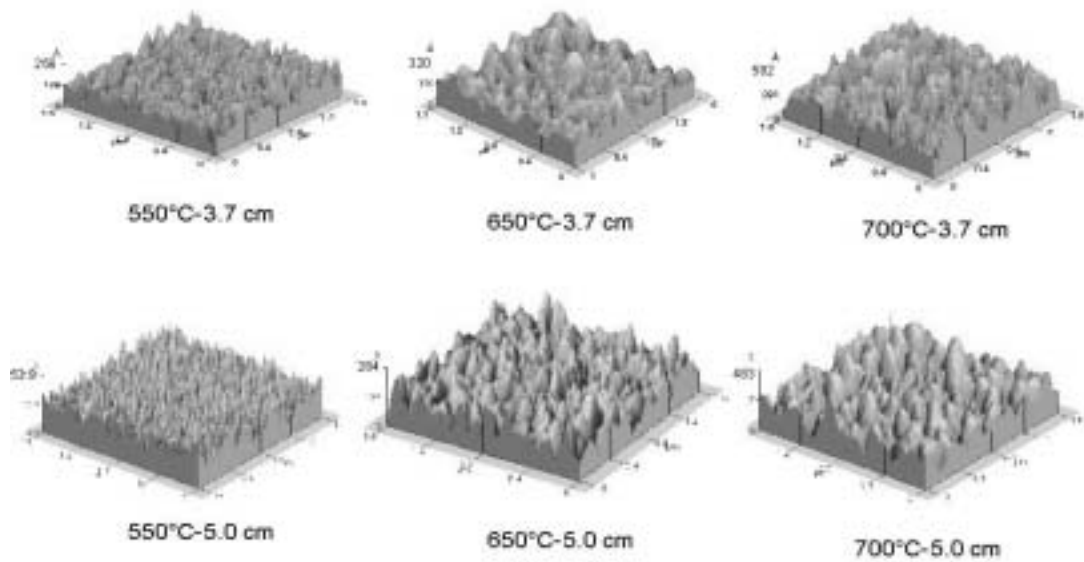


Fig. 12. AFM images of LCCO films deposited at different temperatures and target-substrate distances (note the different height scales).

The changes of the structural dimensions can be explained by the higher mobility of the arriving particles and clusters due to the higher energy (either kinetic or thermal from the substrate). The description of the structures according to Thornton's model is more complicated, as all resemble the above described mixture between zone T and zone I, with the possible exception of the film grown at 550°C at a distance of 5.0 cm. The morphology of this film can probably be described as a zone I structure. This suggests that in principle zone I structures are obtained by PRCLA, only at low temperature and kinetic energies. Another possible parameter that must be considered is the energy of the excited state species in the plasma. Optical observation of the plasma during PRCLA suggests that the plasma extends much further from target and is much brighter than in the case of normal PLD. It is therefore quite probable that a pronounced amount of excited states species will also arrive at the substrate, thus adding to the energy balance of the growing film.

Time- and space-resolved emission spectroscopy measurements were performed to understand and quantify the role of the kinetic energy and plasma expansion characteristics (excited states). A comparison of the emission spectra for PLD (with a low background pressure) and PRCLA is presented in Fig. 13. The emission spectrum for PRCLA reveals a much higher intensity than the PLD spectrum.

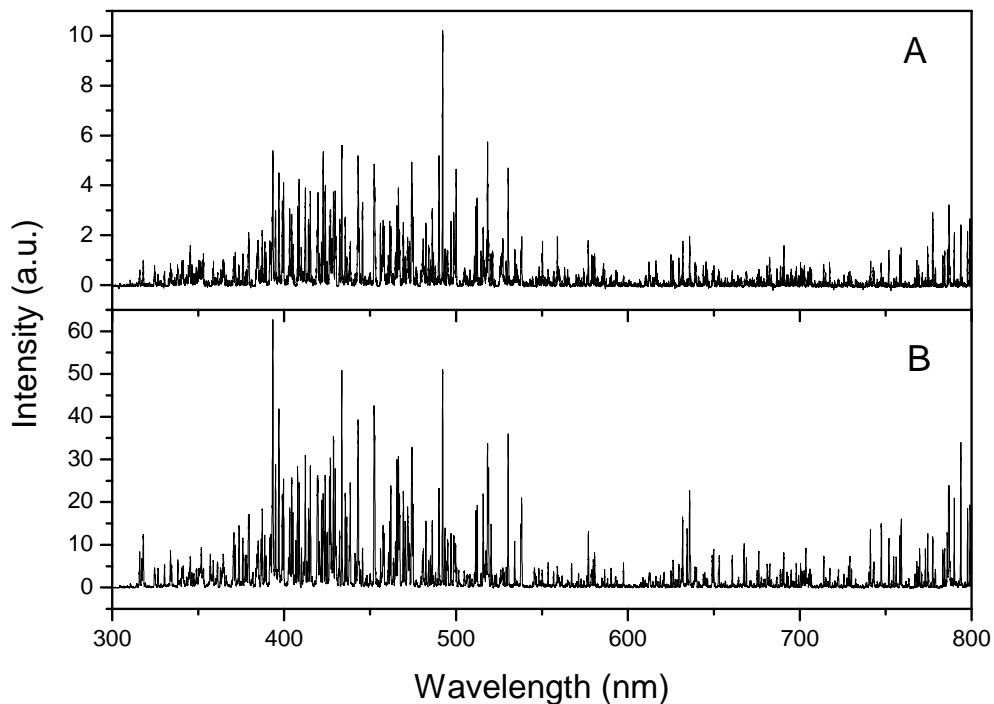


Fig. 13. Emission spectra of LCCO ablation A: oxygen background PLD and B: PRCLA.

This increase in intensity is even more pronounced for the lines in the region between 370-450 nm (ultraviolet), which are associated with higher ionization states of La, Ca and Co. This indicates that a larger amount of (excited) ionic species will arrive at the substrate, which may also influence the surface morphology. Peaks due to nitrogen and oxygen have in general a very low intensity and can not be detected clearly (also due to the overlap with strong lines from the metals). The detailed spectral analysis is based on the most intense lines which can be clearly assigned to one element [61].

The influence of the distance (space) and time (temporal) on the emission spectra are shown in Fig. 14. The decay of the excited species in the presence of oxygen shows nearly an exponential decay (Fig. 14 left). When the gas pulse is present this decay occurs further away from the target. In the proximity of the target (0-2 mm) which corresponds probably to the main interaction zone of the gas pulse with the plasma, a slight decay is observed which is followed by a fast decay. The nearly constant intensity of the plasma species close to the target can be assigned to an equilibrium between the decay (de-excitation) and the formation of new excited states species from the collision between the gas molecules and the ablated atoms. After this collision zone the spontaneous emission becomes predominant. The analysis of the time-distance relation of the maximum intensity reveals clearly that higher intensities are observed for PRCLA, but also that the maximum intensity can be observed until later times (Fig. 14 right, i.e. increasing distance).

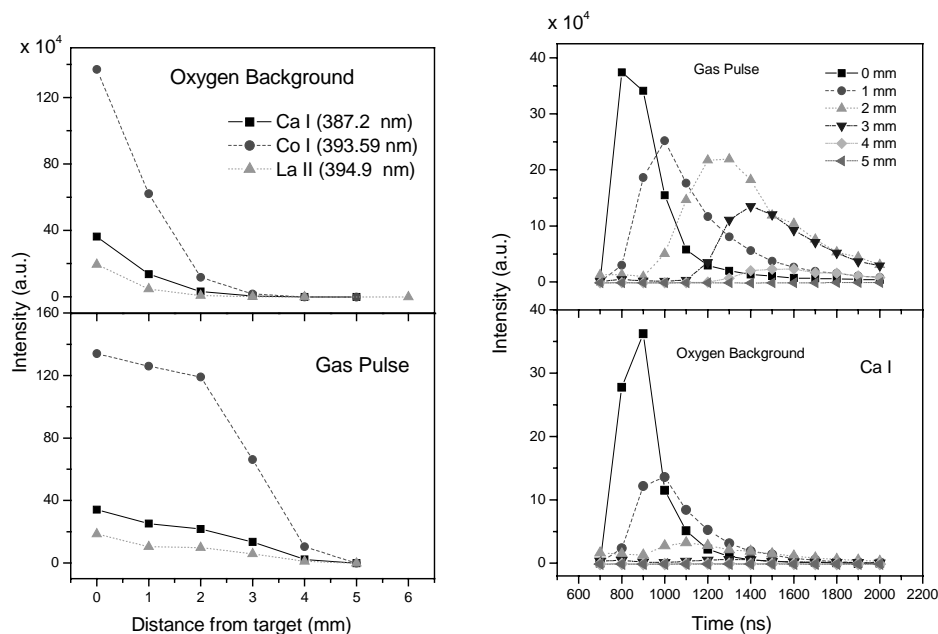


Fig. 14. Spatial (left) and temporal (right) evolution of peak maxima of various plasma species.

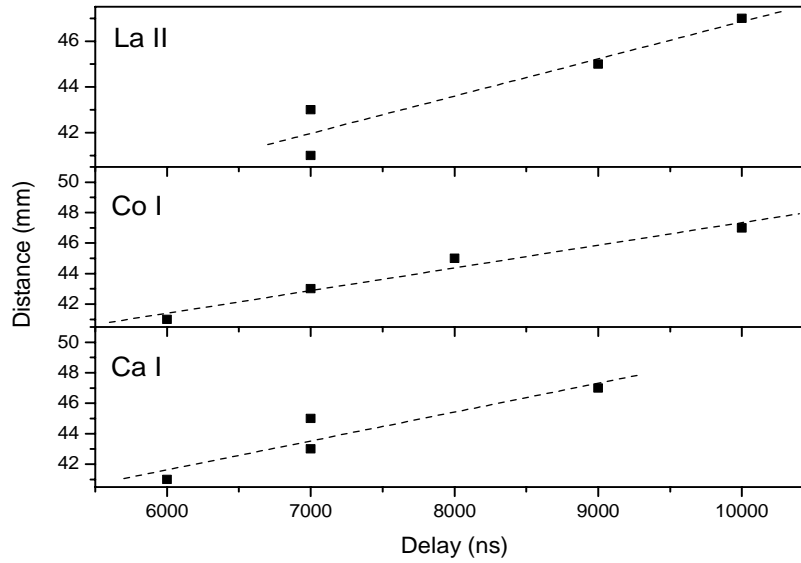


Fig. 15. Velocities of Ca I, Co I and La II plasma species

A comparison of the excited states species lifetime [62] (in the range of several ns to  $1\mu\text{s}$  for Ca I) with the timescale of the maximum emission (up to  $1.5\mu\text{s}$ ) indicates that the species are created significantly after the ablation, in the interaction zone with the gas pulse.

The kinetic energy of the arriving atoms can be calculated from the emission spectra after determining the velocity of the plasma particles (Fig. 15). The kinetic energies were calculated from the slopes of the distance-delay plots in Figure 15 and are compiled in Table 3.

Table 3

Calculated kinetic energy for different atoms of LCCO.

Atoms	Velocity (m/s)	Kinetic energy (eV)
Ca I	1890	0.74
Ca II	2000	0.83
Co I	1490	0.678
Co II	2550	1.99
La II	1630	1.92

These values strongly suggest that the atoms which arrive at the surface have not enough kinetic energy to cause re-sputtering (typically observed for kinetic energies of  $\gg 10$  eV). This explains also the constant composition of the films over a wide range of target–substrate distances. This low kinetic energy compared to normal PLD (1 to 100 eV, but with the possibility of energies of up to 1 keV) [63] is due to the large number of collisions which occur in the initial interaction zone (around 10 times more collisions than for PLD) [62]. The analysis of the time and space resolved emission spectra reveal several pronounced differences of PRCLA compared to PLD:

- Lower kinetic energies of species arriving at the substrate.
- Larger amount of excited states species arriving at the substrate.
- Larger amount of (excited) ionic species arriving at the substrate.

Probably these are also the reasons why the surface morphologies deviate from Thornton's model.

The last step in our study was to apply the knowledge obtained from the above described experiments to control the deposition of the LCCO films precisely and thus obtain films that can be applied as model system for our electrochemistry studies. These selected films were carefully characterised prior to the electrochemical measurements, e.g. concerning oxygen stoichiometry, crystallographic structure, and surface composition. Various gas diffusion electrodes were analysed to allow a comparison and evaluation of our model systems. The polarization curves of these gas diffusion electrodes are shown in Figure 16.

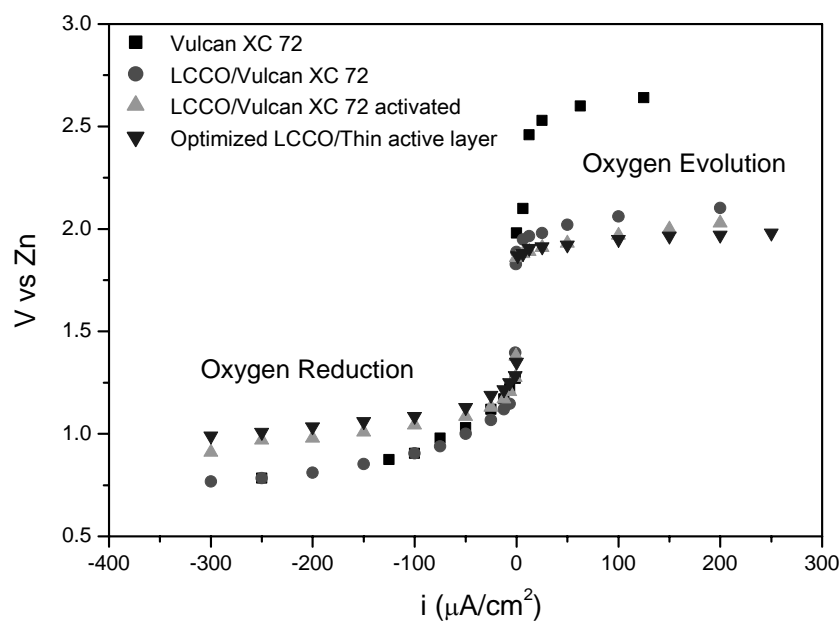


Fig. 16. Polarization curves for different gas diffusion electrodes.

These polarization curves clearly emphasize the advantage of studying model systems, as a clear activity for carbon (Vulcan XC 72) is observed. The overpotential for the two oxygen reactions is quite high (approx. 1.5 V). The overpotential is significantly reduced to approximately 800 mV after the catalyst (LCCO) is added to the carbon. This proves an activity enhancement of the electrode due to the catalyst which is most pronounced for the oxygen evolution reaction. Additional optimisation of the electrode for stability and catalytic activity was performed, i.e. activation of the carbon at high temperatures (high surface and high porosity) and optimisation of the thickness of the gas diffusion electrode. This optimized electrode is up to now the best performing electrode for Zn/air batteries.

This optimized electrode was chosen as a reference to be compared with our model system, i.e. films produced by PRCLA. Two films were selected as films for these study (a polycrystalline film deposited on stainless steel and a single crystalline deposited on MgO(100)). The results are presented in Figure 17. The polarization curves show that the model systems present a slightly smaller overpotential for the two oxygen reactions than the optimized gas diffusion electrode. The model system is more active for the oxygen evolution reaction while the gas diffusion electrode is more active for the oxygen reduction reaction. The single crystalline film on MgO reveals a higher current density at the same voltage than the polycrystalline film on stainless steel. This effect of the crystallinity of the LCCO is more pronounced for the oxygen reduction reaction, and has to our knowledge not been observed previously.

Further experiments are in progress to produce thin film of other perovskite materials. These will be compared with the “real” electrodes, in order to understand the differences in activity for the different materials and crystallographic features.

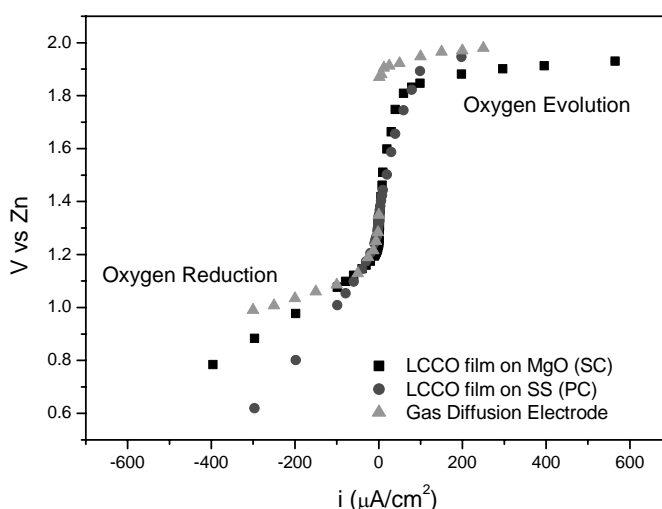


Fig. 17. Polarization curves for different electrodes: PRCLA films as model system and the optimised gas diffusion electrode.

## 4. CONCLUSIONS

The application of PRCLA as deposition technique confirms the possibility to produce thin films of perovskite-type oxide materials without oxygen deficiencies and without additional processing steps (e.g. annealing). The low kinetic energy of the atoms/species arriving at the substrate surface prevents re-sputtering, which allows to grow films with the same composition than the target material, in a variety of target-substrate distances. The crystallinity of the films can be controlled from amorphous to single crystalline, by varying the substrate temperature, the substrate material, its orientation, and the distance between target and substrate. The initial studies have already revealed that the crystallinity has a pronounced influence on the catalytic activity. The surface morphology of the films can be controlled as well by selecting the deposition parameters. The morphology of the films can not be directly described with existing models, most probably due to the additional influence of parameters, e.g. plasma expansion /duration and amount of excited ionic species, which are specific to PRCLA.

Finally, the films produced by PRCLA prove the possibility to apply thin films as model systems for electrochemical studies. Future studies will be aimed at the optimisation of the catalyst and understanding of the catalytic mechanisms, e.g. the role of the crystalline structure.

## ACKNOWLEDGEMENTS

The authors thank Paul Scherrer Institut for financial support and are grateful to Dr. Max Döbeli for the RBS measurements and discussions, and to P.R. Willmott for his help during the experiments and interesting discussions.

## REFERENCES

- [1] F.S. Galasso, Structure, Properties and Preparation of Perovskite-type Compounds, Pergamon Press, London, 1969.
- [2] C.D. Chandler, C. Roger and M.J. Hampden-Smith, Chem. Rev. 93 (1993) 1205.
- [3] A.F. Wells, Structural Inorganic Chemistry, Oxford Science Publications, Clarendon Press, Oxford, 1986.
- [4] L.G. Tejuca, J.L.G. Fierro, and J.M.D. Tarascon, Advances in Catalysis, D.D. Eley, H. Pines, and P.B. Weisz (eds.), Academic Press, New York, 1989.
- [5] H. Song, W. Kim, S.J. Kwon and J. Kang, J. Appl. Phys., 89 (2201) 3398.
- [6] J.T. Cheung, P.E.D. Morgan, D.H. Lowndes, X.Y. Zheng and J. Breen, Appl. Phys. Lett 62 (1993) 2045.
- [7] S. Müller, F. Holzer and O. Haas, J. Appl. Electrochem. 28 (1998) 895.
- [8] Y. Shimizu, K. Uemura, H. Matsuda, N. Miura and N. Yamazoe, J. Electrochem. Soc. 137 (1990) 3430.
- [9] C. Fierro, R.E. Carbonio, D. Scherson and E.B. Yeager, Electrochim. Acta, 33 (1988) 941.

- [10] A. Weidenkaff, S.G. Ebbinghaus and T. Lippert, *Chem. Mat.*, 14 (2002) 1797.
- [11] P.N. Ross and M. Sattler, *J. Electrochem. Soc.*, 135 (1988) 1464.
- [12] J. Prakash, D. Tryk and E. Yeager, *J. Power Sources*, 29 (1990) 413.
- [13] J. Prakash, D. Tryk, W. Aldred and E. Yeager, *Electrochemistry in Transition*, O.J. Murphy, S. Srinivasan and B.E. Conway (eds.), Plenum Press, New York, 1992.
- [14] Y.-F. Yang and Y.-H. Zhou, *J. Electroanal. Chem.*, 397 (1995) 271.
- [15] A.M. Kannan, A.K. Shukla and S. Sathyanarayana, *J. Power Sources*, 25 (1989) 141.
- [16] J.O.M. Bockris and T. Otagawa, *J. Electrochem. Soc.*, 131 (1984) 290.
- [17] S. Müller, K. Striebel and O. Haas, *Electrochim. Acta*, 39 (1994) 1661.
- [18] M. Tsionsky and O. Lev, *ibid.*, 142 (1995) 2132.
- [19] C. Fischer, N. Alonsovante, S. Fiechter and H. Tributsch, *J. Appl. Electrochem.*, 25 (1995) 1004.
- [20] R.E. Carbonio, C. Fierro, D. Tryk and E. Yeager, *J. Power Sources*, 22 (1988) 387.
- [21] R.N. Singh, N.K. Singh and J.P. Singh, *Electrochim. Acta*, 47 (2002) 3873.
- [22] T. Horita, K. Yamaji, N. Sakai, H. Yokokawa, A. Weber and E. Ivers-Tiffée, *Electrochim. Acta*, 46 (2001) 1837.
- [23] H. Tamara, H. Yoneyama and Y. Matsumoto, in *Electrodes of Conductive Metallic Oxides*, S. Trasatti (ed.), Elsevier, New York, 1980.
- [24] A.K. Shukla, A.M. Hannan, M.S. Hedge and J. Gopalakrishnan, *J. Power Sources*, 35 (1991) 163.
- [25] G.P. Luo, Y.S. Wang, S.Y. Chen, A.K. Heilman, C.L. Chen, C.W. Chu, Y. Liou and N.B. Meng, *Appl. Phys. Lett.* 76 (2000) 1908.
- [26] N.-L. Wu, W.-R. Liu, S.-J. Su, *Electrochim. Acta*, 48 (2003) 1567.
- [27] J.B. Goodenough and R. Manoharan, *Electrochemical Society Proceedings*, 92 (1992) 11.
- [28] K. Kinoshita, *Electrochemical Oxygen Technology*, John Wiley & Sons, New York, 1992.
- [29] H.S. Wang, D. Eissler, Y. Kershaw, W. Dietsche, A. Fischer, K. Pllog and D. Brunner, *Appl. Phys. Lett.* 60 (1992) 778.
- [30] C. Dubourdieu, M. Rosina, H. Roussel, F. Weiss, J.P. Sénateur and J.L. Hodeau, *Appl. Phys. Lett.* 79 (2001) 1246.
- [31] T.G. Souza Cruz, M.U. Kleinke and A. Gorenstein, *Appl. Phys. Lett.* 81 (2002) 4922.
- [32] V.G. Prokhorov, Y.P. Lee, K.W. Kim, V.M. Ishchuk and I.N. Chukanova, *Appl. Phys. Lett.* 80 (2002) 2353.
- [33] F.J. Cadieu, L. Chen, B. Li and T. Theodoropoulos, *Appl. Phys. Lett.* 87 (2000) 6770.
- [34] R. Rauer, J. Bäckström, D. Budelmann, M. Kurfiß, M. Schilling, M. Rübhausen, T. Walter, K. Dörr, and S.L. Cooper, *Appl. Phys. Lett.* 81 (2002) 3777.
- [35] D.B. Chrisey and G.K. Hubler (eds), *Pulse Laser Deposition of Thin Films*, John Wiley & Sons, New York, 1994.
- [36] P.R. Willmott and J.R. Huber, *Rev. Mod. Phys.* 72 (2000) 1.
- [37] D. Bäuerle, *Laser Processing and Chemistry*, Springer Verlag, Berlin, 2000.
- [38] T. Kobayashi, H. Akiyoshi and M. Tachiki, *Appl. Surf. Sci.* 197-198 (2002) 294.
- [39] A. Giardini, V. Marotta, A. Morone, S. Orlando and G.P. Parisi, *Appl. Surf. Sci.* 197-198 (2002) 338.
- [40] C. Vivien, M. Dinescu, P. Meheust, C. Boulmer-Leborgne, A.P. Caricato and J. Perriere, *Appl. Surf. Sci.* 127-129 (1998) 668.
- [41] A. Narazaki, T. Sato, Y. Kawaguchi, H. Niino, A. Yabe, T. Sasaki and N. Koshizaki, *Appl. Surf. Sci.* 197-198 (2002) 438.
- [42] V. Craciun, D. Craciun, Z. Chen, J. Hwang and R.K. Singh, *Appl. Surf. Sci.* 168 (2000) 118.

- [43] J.W.Yoon, T. Sasaki and N. Koshizaki, *Appl. Phys. A* 76 (2003) 641.
- [44] G. Radhakrishnan and P.M. Adams, *Appl. Phys. A* 69 (1999) 33.
- [45] M.J. Montenegro, M. Döbeli, T. Lippert, S. Müller, B. Schnyder, A. Weidenkaff, P.R. Willmott and A. Wokaun, *Phys. Chem. Chem. Phys.* 4 (2002) 2799.
- [46] A. Gupta and B.W. Hussey, *Appl. Phys. Lett.* 58 (1991) 1211.
- [47] P.R. Willmott and F. Antoni, *Appl. Phys. Lett.* 73 (1998) 1394.
- [48] M.J. Montenegro, T. Lippert, S. Müller, A. Weidenkaff, P.R. Willmott and A. Wokaun, *Appl. Surf. Sci.* 197-198 (2002) 505.
- [49] S. Müller, K. Striebel and O. Haas, *Electrochim. Acta*, 39 (1994) 1661.
- [50] S. Müller, F. Holzer, O. Haas, C. Schlatter and C. Comminellis, *Chimia* 49 (1995) 27.
- [51] S. Müller, O. Haas, C. Schlatter and C. Comminellis, *J. Appl. Electrochem.* 28 (1998) 305.
- [52] F.J. Morin, and J.P. Mauta, *Phys. Rev.* 96 (1954) 28.
- [53] L.R. Doolittle, *Nucl. Instrum. Methods B*15 (1986) 227.
- [54] H. Arai, S. Müller and O. Haas, *J. Electrochem. Soc.* 147 (2000) 3584.
- [55] I.W. Boyd and W. Zhang, *App. Surf. Sci.*, 168 (2000) 53.
- [56] V. Craciun, D. Craciun, J. Perriere and I.W. Boyd, *J. Appl. Phys.* 85 (1999) 3310.
- [57] T. Scharf and H.U. Krebs, *Appl. Phys. A* 75 (2002) 551.
- [58] J.A. Thornton, *J. Vac. Sci. Technol. A* 4 (1986) 3059.
- [59] M. Koubaa, A.M. Hanghiri-Gosnet, R. Desfeux, Ph Lecoeur, W. Prellier and B. Mercey, *J. Appl. Phys.* 93 (2003) 5227.
- [60] A. Gupta, B.W. Hussey and M.Y. Chern, *Physica C* 200 (1992) 263.
- [61] R.C. Weast, M.J. Astle and W.H. Beyer, *Handbook of Chemistry and Physics*, CRC Press, Boca Raton, FL, 1988.
- [62] M.J. Montenegro, C. Clerc, T. Lippert, S. Müller, A. Weidenkaff, P.R. Willmott and A. Wokaun, *Appl. Surf. Sci.* 208-209 (2003) 45.
- [63] H.-J. Dang, Q.-Z. Qin, *Chem. Phys. Lett.* 354 (2002) 210.